Kumar Pankaj (Orcid ID: 0000-0003-1906-9852)
mallick subrat kumar Kumar (Orcid ID: 0000-0002-5453-4708)
Dubey Aditya Kumar (Orcid ID: 0000-0003-0579-9109)
Cabos William (Orcid ID: 0000-0003-3638-6438)

Regional Earth System Model for CORDEX-South Asia: a comparative assessment of RESM and ESM over the tropical Indian Ocean

Pankaj Kumar[*1], Subrat Mallick[1], Alok Kumar Mishra[1], Aditya Kumar Dubey[1], Gaurav Tiwari[1], Dimitry V. Sein[2,3], William Cabos[4], Daniela Jacob[5]

[1]Department of Earth and Environmental Sciences, Indian Institute of Science Education and Research, Bhopal, India

[2]Shirshov Institute of Oceanology, Russian Academy of Sciences, Moscow, Russia

[3]Alfred Wegener Institute for Polar and Marine Research, Bremerhaven, Germany

[4]University of Alcala, Spain

[5] Climate Service Center, Germany

Corresponding author: Pankaj Kumar

Email: kumarp@iiserb.ac.in

Department of Earth and Environmental Sciences

Indian Institute of Science Education and Research Bhopal, Bhopal-462066, India

Abstract

Understanding climate variability requires good quality high resolution spatially and temporally varying ocean fields due to its decisive role in regulating the region's climate, including the Indian summer monsoon. In this regard, we employed a new high-resolution regional earth system model (RESM), namely ROM over CORDEX South Asia. We demonstrated the performance of the RESM and its added value over the global earth system model, namely MPI-ESM, in simulating the hydrographic characteristics and associated mechanism over the tropical Indian Ocean (TIO). ROM shows better skill than MPI-ESM in simulating the near-surface and subsurface characteristics of the ocean. However, larger added values are noticed for subsurface (>350m) thermal structure. MPI-ESM's cold sea surface temperature (SST) bias is reduced in ROM which is associated with weaker winds, anomalous cyclonic wind stress curl, enhanced stratifications, and a shallower mixed layer, resulting in greater upper-ocean heating. The reduced SST bias is also consistent with improved ocean meridional heat transport (OMHT) in ROM. For example, reduced southward export of OMHT over the Arabian Sea increases the surface warming by ~4%, reducing the RMSE by ~0.2°C - 0.6°C and becoming closer to observation. The anomalous cyclonic wind stress curl, in turn, caused mixed layer stratifications in the western Indian Ocean. The advective heat transfer from the south-eastern Indian Ocean to the western Indian Ocean reduced oceanic cooling by vertical processes, overcame the cooling by the net loss of surface heat fluxes, and favored the TIO's surface warming.

Keywords: Tropical Indian Ocean, Regional Earth System Model, Dynamical and thermodynamical processes

1 Introduction

The tropical Indian Ocean (TIO) plays an active role in the natural variability of the climate system over South Asia, eastern tropical Africa, and western Australia (Annamalai and

Murtugudde 2004; Schott et al., 2009). Seasonal variations of near-surface ocean thermal structure set the platform for thermodynamical changes between ocean and atmosphere in TIO. The strongest impacts are related to changes at the surface boundary layer, which cause a significant change in fluxes and modes of climate variability. The air-sea flux variability over TIO influences climate on both regional and global scales (Behera et al., 1999; Yamagata et al., 2004).

Regional-scale air-sea interaction and feedback processes are fundamental to control the ocean variability over TIO and Indian summer monsoon rainfall (ISMR) (Schott and McCreary, 2001; Vinayachandran et al., 2015; Srivastava et al., 2018). In turn, the SST influences the atmospheric boundary layer and modifies the moist atmosphere's temperature profile and atmospheric circulation (Gadgil et al., 1984; Huang et al., 2011). Consequently, the ISMR is influenced by oceanic variability (Roxy et al., 2014; Vinayachandran et al., 2015; Misra et al., 2017; Mishra et al., 2020). Therefore, it is crucial to understand the impact of regional air-sea coupling (air-sea interaction) in simulating the circulation and variability of TIO, which is one of the objectives of this study.

The warming of the TIO under global warming has been reported in earlier studies (Roxy et al., 2014). It is believed that the intensification of TIO warming alters Asian monsoon variability and further affects the climates over the Indian Ocean (IO) rim countries (Abram et al., 2008; Cai et al., 2014; Dong et al., 2014). For instance, an increase in TIO surface warming leads to strong upper-ocean stratification and reduces mixing. In turn, changes in mixed layer (ML) modulate the subsurface temperature and ocean heat storage (Shroyer et al., 2016). Saji et al., (1999) and Lau and Waliser (2011) reported that a strong warming trend in TIO accelerates several modes of intra-seasonal variability. Recent studies reveal that TIO warming not only reduces the ISMR over India but also reduces rainfall in remote places, for example, over the tropical Atlantic ocean by intensifying the Walker circulation and increasing vertical

stability of the atmosphere (Hu and Fedorov, 2019) and modulates the intensity and frequency tropical cyclones and African, Asian and Australian monsoon system (Delworth et al., 2012).

As stated above, the SST of the northern Indian ocean significantly controls the ISMR (Mishra et al., 2020) and its variability, in particular, the eastward and northward propagation of the convective band (Bellon et al., 2008; Klingaman et al., 2011). Therefore, an accurate estimation of SST is very crucial. Furthermore, as the SST is significantly controlled by upper-ocean thermodynamics, an adequate estimation of the subsurface ocean is also important. Various studies employed the high-resolution regional ocean models to investigate the circulation and variability of the Indian ocean (Huang et al., 2015; Srivastav et al., 2016, 2018; Dwivedi et al., 2018, 2019; Benshila et al., 2014; Pandey and Dwivedi, 2021). Most of these studies have shown the advantage of high-resolution modeling to improve the Indian Ocean's variability. However, the stand-alone ocean models lack the air-sea interactions, which profoundly impact the dynamics of TIO and hence global and regional climate systems (Trenberth and Solomon, 1994; Zheng and Giese, 2009). These demands improving the understanding of the dynamical and thermodynamical properties of the Indian Ocean using a high-resolution coupled atmosphere-ocean model or RESM, which is one of the objectives of this study.

Coupled Earth System Models (ESMs) are the most sophisticated tool to investigate global climate and individual components of the climate systems, including atmosphere, ocean, land, and their driving plausible mechanisms. They usually assist in inspecting the related mechanisms of dynamics and thermodynamics of the complex climate system (Stathopoulos et al., 2020). The spatially coarse resolution (which is not less than 100km up to now) of ESMs is one of the fundamental sources of strong biases in the SST and salinity field, which affects the physical state of the ocean's subsurface and air-sea fluxes (Ma et al., 2015; Chassignet et al., 2020), limiting the predictive skill ESMs to predict the ISMR. Therefore, high-resolution

ESMs are necessary for improving the simulated ocean state over TIO and hence ISMR. However, it is computationally expensive, and alternatively, high-resolution RESM can be used at a less computational cost. Various RESM having varying complexities have been developed and employed to explore the understanding of atmospheric and oceanic variability over different regions of the globe and suggest improvements (Sein et al., 2015; Wang et al., 2015; Dubey et al., 2021; Mishra et al., 2021a,b; Saharwardi et al., 2021; Kumar et al., 2022; Mishra et al. 2022a,b,c). Kumar et al (2022) demonstrated that dynamical and thermodynamical processes including the upper tropospheric circulation associated with the Indian summer monsoon employing the same model used in this study. Comparatively lesser efforts have been made over TIO (Samson et al., 2015).

In this study, an effort is made to perform high-resolution regional earth system modeling using a new RESM, namely ROM, to improve TIO characteristics. To compute the added value of ROM over global ESM, we compare the ocean fields simulated by ROM and the earth system model, namely MPI-ESM, for the period 1982-2001. The details of the simulations are well described in the model component/description section.

2 Model description

This study employed a high-resolution regional earth system model (RESM), namely ROM, which consists of several components of the climate systems (i.e. Atmosphere-Ocean-land-hydrology and biogeochemistry). The ocean fields simulated by ROM are compared with those from a simulation with global the earth system model having low resolution (having 1.8653º and 1.875º in longitude and latitude) hereafter MPI-ESM. MPI-ESM consists of ECHAM6 (Stevens et al., 2013) for the atmosphere component, Max Planck Institute Ocean Model (MPIOM) (Jungclaus et al., 2006) for the ocean, and Hydrological Discharge model (HD) (Hagemann and Dümenil, 1997). The same ocean component is also adopted in our ROM setup, which is formulated with the hydrostatic approximation covering the global domain,

which makes it different from the conventional regional earth system models (generally utilized regionally configured ocean model), which have an additional source of uncertainty (i) coming from the unrealistic lateral boundaries (LB) (Sein et al., 2020). (ii) uncertainty on the influence of coastal waves originating from outside the target region (beyond coupled domain consisting regional ocean model). The use of the global ocean model overcomes these complications, which brings important advantages for climate change scenario simulations. Over the open Ocean of Indian Ocean, horizontal is taken as ~20km, which further increased up to 10 km (eddy-permitting) over the coastal region and decreased gradually, reaching a minimum of 100 km in the southern seas. We use 40 unevenly spaced vertical z-levels and incorporate the influence of ocean tides. The MPIOM uses bottom boundary layer slope convection (Marsland et al., 2003) and an isopycnal diffusion scheme (Griffies, 1998). The model is also equipped with tidal forcing, derived from the full ephemerides lunisolar tidal potential (Thomas et al., 2001). The ocean model receives continental runoff from the global HD model and delivers freshwater discharge at the exact river mouth. The regional atmosphere model REMO (Jacob 2001) having a horizontal resolution of 25 km, which is coupled over the CORDEX South Asia domain (https://www.cordex.org/) (Sein et al., 2015) (Figure 1). In both simulations, the models are coupled via an OASIS coupler (Valcke et al., 2013).

The MPI-ESM historical simulation was initialized from a preindustrial control run (PI-Control) and ran for the period 1850-2005. The data obtained from Polar Science Center Hydrographic Climatology (PHC) is used initialized ocean component of RESM. It thereafter ran in the spin-up mode for 90 years cyclically with ERA-40 reanalysis forcing (2 times for 45 years, from 1958 to 2002). In addition, surface salinity fields of ROM were relaxed to monthly climatological values with a relaxation constant 1/180 days. This allowed us to keep the annual cycle. Considering the relaxation time 180 days, the relaxation term for the upper layer in the

salinity equation looks like c*(S-Sobs), where Sobs is observed monthly mean climatology of sea surface salinity and c is relaxation constant (in our case 1/180 days, i.e. 1/(180*24*3600). The ROM spin-up and salinity restoring procedures are described in detail in Sein et al., (2015, 2020, 2022). Both ROM and MPI-ESM have identical ocean model physics but differ in grid resolution and input forcings. The monthly outcomes of both simulations were analyzed for the period 1982-2001.

3   Data methodology

The monthly average of ~25km National Oceanic and Atmospheric Administration (NOAA) Optimum Interpolation Sea Surface Temperature (OISST) was used to evaluate simulated SSTs. The analyzed OISST has been produced using the optimal interpolation technique (Reynolds et al., 2007). The monthly average of Centro Euro-Mediterraneo sui Cambiamenti Climatici (CMCC) Global Ocean Reanalysis System (C-GLORS; version 5) ML was used to evaluate the corresponding simulated values. The reanalyzed monthly C-GLORS ML product has been developed using the three-dimensional variational (3DVar) data assimilation technique (Storto and Masina 2016). The reanalysis product of the monthly C-GLORS ML field was obtained from climate-data-guide (https://climatedataguide.ucar.edu/climate-data). The monthly average of ~33km Ocean Surface Current Analysis Real-time (OSCAR) (Bonjean and Lagerloef 2002) was used to evaluate simulated surface current velocity. The OSCAR currents were obtained from the Physical Oceanography Distributed Active Archive Centre (PODACC) (https://podaac.jpl.nasa.gov/dataset/OSCAR_L4_OC_third-deg).   The   profile temperatures of the Indian Ocean under the Global Temperature and Salinity Profile Programme (GTSPP) (Sun, C. & Co-Authors (2010)) were used for the evaluation of simulated water temperature. The GTSPP profiles were obtained from the National Oceanographic Data Centre (NODC) (https://www.nodc.noaa.gov). The oceanic surface wind stress of the TROPFLUX (tropical ocean tropical flux) analysis (Praveen et al., 2013) was used to evaluate

the model results. This analyzed wind stress product is obtained from the Indian National Centre for Ocean Information Services (INCOIS) (https://incois.gov.in/tropflux/)

The models' accuracy in the representation of the thermal structure is evaluated by calculating bias, mean, standard deviation (STD), root-mean-square-error (RMSE), correlation, and the percentage change in the RMSE (see eq. 1) between the runs with respect to observations is addressed in the study. The oceans' meridional heat transport (OMHT; see eq. 2) are computed using the formulation of Mallick et al. (2020) and Zheng and Giese (2009).

$$Added\ value\ (AV) = \left[\frac{(RMSE_{MPI-ESM-LR} - RMSE_{ROM})}{RMSE_{MPI-ESM-LR}} \right] \times 100 \qquad (1)$$

$$OMHT = \int_{west}^{east} \int_{-H}^{0} \rho\ C_p\ \upsilon\ T_{(z)} dz\ dx \qquad (2)$$

where RMSE is the root mean square error of simulated SST with respect to Reynolds OISST, x is the coordinate in the east-west direction, z is the vertical coordinate, $T_{(z)}$ is the simulated oceans' water temperature (WT), υ is the meridional current velocity, C_p is the seawater thermal capacity under constant pressure, ρ is the oceans' water density, and H is the depth of the ocean.

4   Results

In this section, we demonstrated the skill of the ROM simulated fields (e.g. SST, ML, sea surface hight anomaly (SSHA), and ocean surface current (OSC)) and added value over global MPI-ESM in our study region (20°S – 30°N, 30°E – 120°E). To discuss the model validation against the observations, we compare the annual mean of the modeled SST, ML, surface wind stress (SWS), and OSC against the datasets described above. We also discuss the annual cycle of OMHT, SST, SSHA, zonal velocity, and OSC magnitude. The SST is validated with Reynolds OISST, ML is validated with CGLORS v5 ML, SWS is validated with TROPFLUX,

OSC is validated with OSCAR current, SSHA is validated with altimeter derived SSHA (ALTI), and simulated profile WT is validated with GTSPP profile temperature datasets.

4.1 Sea surface temperature (SST) and its variability

The time-averaged SST bias of both simulations is shown in Figure 2a,b. The oceanic component of MPI-ESM is characterized by a cold SST bias over the entire TIO region. The magnitude of the cold SST bias is maximum over the north-western Arabian Sea (AS) and southwestern Bay of Bengal (BoB) (Figure 2a). These cold SST biases arise due to vertical instability, leading to strong dynamical mixing (deepening of the mixed layer) (Deppenmeier et al., 2020). Interestingly, the cold SST bias over the AS and Southern TIO is significantly reduced in ROM (Figure 2b), however, it shows a positive SST bias of ~0.6°C and above concentrated in the western AS (AS; 10°N – 25°N and 45°E – 78°E), and western equatorial Indian Ocean (WEIO; 5°S – 5°N and 35°E – 60°E) (Figure 2b). The positive SST bias over the western AS and WEIO in ROM is because of shallowing of mixed layer and accumulation (or pile-up) of warm water mass at the western frontier of the eastern equatorial Indian Ocean (EIO), which is advected from the eastern region of the EIO (this is discussed broadly in the later sub-section of the manuscript).

To make a quantitative comparison of both simulations in simulating SST, we computed the difference between SST simulated by ROM and MPI-ESM (Figure 2c). The magnitude of SST in the southern Indian Ocean (SIO; 20°S – 5°S and 40°E – 110°E) is increased by ~0.4°C while it is decreased over the eastern region of BoB and eastern EIO (EEIO; 5°S – 5°N and 95°E – 105°E). The decrease of SST (enhanced surface cooling) is due to stronger positive feedback between equatorial easterlies, upwelling, and coastal Kelvin waves (Fischer et al., 2005). However, in the WEIO, the convergence of advected warm surface water from EEIO enhance the surface warming by ~0.6°C – 1.0°C in WEIO and cooling by ~0.1°C-0.2°C in EEIO in ROM compared to MPI-ESM, representing ~3% enhancement in the

west and ~0.5% reduction in the east. In ROM, the magnitude of area average SST in the AS, WEIO, and SIO basins is increased by ~1.4°C, ~0.9°C, and ~0.4°C, respectively. However, in the eastern regime of BoB and EEIO, the domain average SST magnitude is reduced by ~0.2°C and ~0.1°C, respectively. In the AS, WEIO, SIO, and some parts of the BoB, the magnitude of SST increases by ~ 6%, ~3%, 1.4%, and 0.5%, respectively.

To make results more perspective, we investigated the model's potential in simulating the SST over different subregions (AS, BoB, EIO, SIO) of the Indian ocean using different performance matrice i.e., root mean square error (RMSE) and the standard deviation (SD). The RMSE between model and observation is less than the SD of observation demonstrating the good quality of the model data (Srivastava et al., 2016, 2018). We tabulated the performance matrice in the table. From the table, it is noticed that the RMSE in SST is less than the standard deviation of observation in both ROM over all regions is less than the observation, demonstrating the quality of ROM's simulated SST. Furthermore, the RMSE in the ROM's SST is notably less than MPI-ESM-LR, clearly depicting the added value over coarse-resolution global model simulation. Both simulations are in good resemblance in simulating the variability (standard deviation) over all regions, however, ROM is relatively closer to observation.

Figure 3 shows the annual mean error of simulated SST and the percentage of improvement (added value) of ROM in simulating SST for 1982 – 2001. Barring a few places, the RMSE is substantially greater in MPI-ESM than ROM. For example, MPI-ESM shows RMSE of ~ 0.8°C – 1.4°C in the AS, SIO, and western regime of BoB (Figure 3a) while ROM shows RMSE of ~0.5°C – 0.6°C over most of TIO, except in the WEIO where the RMSE is significantly larger (Figure 3b). The added value of high-resolution ROM was estimated using eq. (1), and found that ROM shows a substantial added value over MPI-ESM in most of the TIO, where the error

is reduced by ~ 20% – 60%. In contrast to this, some areas of increased error (negative skill) are also noticed over which MPI-ESM performed better than ROM; however, the area and magnitude of the negative skill are minimal than the regions of positive skill.

The investigation annual mean does sufficient to isolate the hidden uncertainty in the different seasons due to compensation in the annual mean. The tropical Indian ocean exhibits substantial seasonal variability driven by near-surface air-sea forcings, in a particular seasonal reversal of wind; thus, it is worth analyzing the model's potential in simulating the SST on the seasonal scale. Therefore we attempted to decipher the ROM's skill and advantage over ESM in simulating seasonal SST. We adopted the season defined by India Meteorological Department. For example, December–January-February; DJF,   March–April-May; MAM, June–July-August-September; JJAS, October-November; ON.

Figure 4 depicts substantial spatio-temporal variability of SST in observation. The highest (lowest) SST is noticed during MAM(DJF).   The higher(lower) solar radiation and shallow(deep) mixed layer depth (figure not shown) are primarily responsible for high(low) SST during MAM(DJF). In general, AS shows lower SST   than   BoB. These features are reasonably captured by ROM and parent ESM; however, the magnitude of ROM's SST is closer to observation than ESM for all seasons and most of the region. On the other hand, over the western coast of AS during JJAS, ESM performed better than ROM.

To make results more perspective, we demonstrated the comparative performance of ROM and MPI-ESM quantitively; seasonal SST bias is computed (Figure S1). The figure reveals substantial spatio-temporal variability in SST bias. In general, MPI-ESM tends to underestimate the SST during all seasons over most of the regions except for some small patches, especially along the coastal area, where overestimation is also noticed. The ROM

shows considerably less underestimation and overestimation during all season except the western coast of AS, where ROM shows stronger bias than MPI-ESM during JJAS.

To assess the model's ability in capturing the spatio-temporal variability of the SST standard deviation for each season using monthly SST data from ROM, ESM, and observation (figure 5). Interestingly, the season of SST value (MAM) exhibits the highest variability over AS followed by during JJAS. The variability is found to be decreased from north to south over AS and BoB during all seasons. MPI-ESM shows reasonable skill in reproducing variability during all seasons with notable magnitude discrepancies. During MAM, MPI_ESM shows stronger variability than observation over AS and BoB, while during JJAS, stronger (weaker) variability is noticed over AS(BoB). This overestimation and underestimation in the variability have substantially reduced the ROM, indicating the advantage of RESM over ESM.

Further, model's skill is evaluated in reproducing the leading modes of the TIO SST variability at interannual time scales. In this regard, EOF analysis is performed using the monthly mean SST for ROM, MPI-ESM, and observation (figure 6). In general, ROM is found to perform slightly better than MPI-ESM. The figure reveals a positive signal over the entire basin in the first EOF mode, indicating the basinwide warming, also known as Indian Ocean basin warming mode (IOBM), in the observations, which is reasonably well simulated by both ROM and MPI-ESM. MPI-ESM shows a slightly stronger positive signal than observation over the eastern IO. The first EOF, the mode in ROM (MPI-ESM), explains ~23% (28%) of the total variance, which is lesser(greater) than the respective values in the observation (25%). The underestimation observed in the ROM is lesser than in a previous study based on CMIP5 models (Du et al., 2013). Though, a direct comparison cannot be made due to different periods of study.

The observed second EOF mode shows a dipole structure, with the positive(negative) signal over eastern(western) IO. ROM generally captures this dipole structure pattern in the second mode with a slight discrepancy in the magnitude of the signal. On the other hand, MPI-ESM shows a contrasting dipole pattern with the negative(positive) signal over eastern(western) IO The second EOF mode in ROM(MPI-ESM)) explains ~ 10% (15%) of the total variance, which is comparable(higher) to that in the observation ~ (10%).

4.2   Oceanic mixed layer (ML)

To investigate the advantage of ROM in simulating the upper ocean stability in the TIO, we estimated the oceanic mixed layer (ML) using the density criterion. The ML is defined as the depth at which density is larger than surface density by $0.125\ kg/m^3$. The study of ML plays a pivotal role in the TIO as it acts as a bridge between the ocean and atmosphere and influences climate change (Yeh et al., 2009; Amaya et al., 2021). Figure 7 displays the time-averaged ML biases for TIO. In MPI-ESM, positive ML bias is concentrated along off Somalia-Kenya-Tanzania region, north of Madagascar, northern parts of EIO, eastern AS, and BoB. Prasad (2004) reported that this positive ML bias is due to wind-induced momentum stress and buoyancy forcing that enhance oceans' convective mixing, leading to deeper ML. On the other hand, negative ML bias is noticed over the south of 10°S (which is the region of higher MLD (figure S2) bias in north-western AS is because of upper-ocean stability. For SIO, the Ekman dynamics associated with wind burst and the precipitation perturbation inhibit the deepening of the ML (Duvel et al., 2004). However, the shoaling of ML in the western BoB is due to the advection of net freshwater flux, causing upper-ocean stratification and the formation of the thick barrier layer (Sharma et al., 2016). In turn, compared to MPI-ESM, the ROM experience a negative ML bias over the TIO (i.e., shallower by 4m – 16m). From the difference in ML of both simulations, it is observed that except for western AS, central and northern parts of BoB, ML (or vertical mixing) in ROM is significantly reduced due to upper-ocean stability. In ROM-

SA, reduction in ML alters the upper ocean thermal structure and increases the ocean heat content in ML, leading to warm the ocean and hence positive SST bias in most of the TIO region (Figure 1b).

Figure 8 shows the annual RMSE of ML for both simulations against observation and the percentage of improvement (added value) for the period 1982 – 2001. It is noted that MPI-ESM shows greater RMSE than ROM. The stronger mixing in MPI-ESM produces deepening ML, hence increasing the positive ML biases (Figure 8a) in the AS, BoB, EIO, and off the African coast. On the contrary, the weaker mixing in ROM also reduces the RMSE in most of the TIO, especially in the BoB, AS, EEIO, and off the African and Madagascar coast (Figure 8b). Additionally, It has been found that ROM improves the ML simulation over most of the TIO except SIO and some patches over AS where performance is degraded. Maximum improvement is observed over eastern AS and some patches along the Somalia coast (~40 %), while 10% - 20% improvement is noticed over the remaining area of the domain (AS and BoB). However, in the SIO, the reduction in vertical mixing increases the ML error by ~20% – 40%.

Further, we demonstrated the skill of ROM as well as MPI-ESM in simulating the ML variability for each season (Figure 9). Observation shows considerable spatial as well as seasonal variability. The AS shows larger variability than BoB for all the seasons; however, notable differences are observed during the winter and summer seasons. The highest variability is observed over the southern Indian Ocean (south of 10°S) during the summer season, followed by MAM. Both models show reasonable skill in distinguishing low and high variability regions. MPI-ESM shows a notable discrepancy in simulating the magnitude of variability. The overestimation (>5-10m) is noticed over the southern Indian Ocean during the summer season and along Sumatra and the Great whirlpool region during winter. These discrepancies are substantially reduced in ROM; however, produce larger bias than MPI-ESM during MAM over northern AS.

4.3 Surface wind stress (SWS)

Figure 10 shows the annual mean surface wind stress (SWS) of the TIO from TROPFLUX (hereinafter referred as TFLX) for both simulations. In northwestern AS, ROM bears quite a resemblance to observation in representing the magnitude of SWS, while MPI-ESM underestimates these values. The lower SWS in MPI-ESM weakens the vertical mixing due to reducing turbulent kinetic energy in northwestern AS and leads to shallow ML with negative bias (Figure 11a). On the contrary, a strong SWS over the eastern region of AS and BoB in MPI-ESM leads to imparting more momentum to the ocean surface. This increases the shear-induced mixing in the water column, increasing the wind-induced ML (Figure 3a-b). The SWS magnitude in MPI-ESM and ROM are well demarcated at the equator (Figure 8b-c); however, MPI-ESM has a stronger SWS (Figure S3), which increases the wind-induced mixing of the equator at a latitudinal band of $0° – 5°N$ and leads to greater positive ML bias. In the SIO, MPI-ESM experienced a stronger SWS magnitude hence ML depth. However, the magnitude of SWS is significantly reduced in ROM, leading to shallow mixing in the SIO.

4.4 Ocean surface current (OSC)

Figure 11 shows the spatial map of the simulated ocean surface current (OSC) that summarizes the annual mean flow of the TIO. Both simulations reproduce well the OSC in the AS, which are in close agreement with the observation (OSCAR), whereas in the BoB, the coastal current is well demarcated in both simulations. It has been found that the magnitude of OSC is much stronger in ROM at the western half of the equator (Figure 11c) while weaker over SIO compared to MPI-ESM. In ROM, the equatorial current is characterized by the westward flow, whereas in MPI-ESM, it shows an eastward flowing equatorial current. The westward equatorial flow advects warm water from the eastern to the western regime of the EIO. It splits at the east coast of Somalia near the equator (0°) into northward and southward branches. The northward branches bring warm water from the WEIO into the AS basin, whereas the

southward branches export to Madagascar's northern tip, where it modulates the upper ocean thermal structure and thereby enhances the SST by 0.2ºC – 0.6ºC (Figure 2b).

During winter (Figure S4), the magnitude of the westward flow of the North Equatorial Current (NEC) becomes much stronger in ROM compared to MPI-ESM and OSCAR. Thereby, a pool of warm surface water is advected and pile-up in the west thereby reducing (increasing) cold SST bias in the WEIO (EEIO). The strength of southward flows of Somali Current (SC) is also enhanced in ROM and meets the East Africa Coastal Current (EACC), then it turns eastward and aligned with South Equatorial Counter Current (SECC). However, in the SIO, the magnitude of the southward flow of ROM current is partially reduced compared to MPI-ESM and OSCAR. This reduction of current velocity reduces the advection of warm surface water and OMHT, increasing the SST over the region.

During summer (Figure S4), the magnitude of the northward flow of Somali Current (SC) is significantly enhanced in ROM compared to MPI-ESM and OSCAR. The increase in the northward flow of SC brings warm surface water from the WEIO into the AS basin, leading to a reduction in southward advection of water mass and OMHT, which leads to a high SST in the AS. In EIO, the magnitude of westward flow equatorial current velocity strongly dominates eastward flow in ROM.

4.5 Simulated vertical profile of water temperature (WT)

The vertical profiles of simulated water temperature (WT) with reference to ARGO have also been analyzed to examine the model's potential to reproduce the vertical thermal structure. The vertical distribution (0m – 1000m) of mean profiles of WT along with standard deviation (STD), root mean square error (RMSE), and correlation for the period of 1985 – 2001 (as per the availability of profile data) are shown in Figure 12. The figure reveals that ROM bears a close resemblance to observation (better than MPI-ESM) in simulating the mean profile. In general, ROM shows added value in simulating the surface as well as subsurface temperature.

However, more considerable value addition is noted for subsurface temperature, especially beyond 350m.

We made a quantitative demonstration by computing the root mean square error (RMSE) for both simulations relative to observation to make results more perspective. It is noted from the profile RMSE that MPI-ESM appears to have serious errors, particularly just below the mixed layer. This could be due to diffused thermocline, which is a common problem in many ocean models. The RMSE is reduced in ROM by 10% (i.e. ~0.2°C) in the top 100m, whereas in the subsurface (beyond 300m), it is significantly reduced by ~30% to 50% (i.e. ~0.6°C – 1.2°C) with maximum reduction at 600m depth of about 60% (i.e. ~1.4°C) (Figure 12c). However, the correlation for ROM is near similar in the top 200m, but the correlation is reduced by ~6% – 8%. This confirms the advantage of using a high-resolution RESM relative to a coarse resolution global model in simulating surface and subsurface thermal structure in the TIO.

4.6 Annual cycle of Oceans' meridional heat transport and SST

The proper stimulation of the annual cycle of ocean fields is a necessary precursor for a potential model that proves the model's ability to simulate the semi-annual variability (which is the dominant mode of variability over TIO). The inaccurate distribution throughout the year leads to altering the Indian summer monsoon, making them unreliable. Thus, it is worthwhile to access the model's performance in simulating the annual cycle. Figure 13 shows the annual cycle of monthly oceans' meridional heat transport (OMHT, in Petawatt (PW), i.e. $1\,PW = 10^{15}\,W$) for both model and corresponding observation. The OMHT of both models for the Arabian Sea (AS), Bay of Bengal (BoB), equatorial Indian Ocean (EIO), and southern Indian Ocean (as marked in Figure 2a) are computed using Eq. (2). The negative (positive) sign corresponds to the southward (northward) export of OMHT (Figure 13a-d). It has been found that the magnitude of southward (northward) export of OMHT varies in different seasons, followed by a variation of SST magnitude (Figure 13e-h). The comparison shows that the

seasonal variation of southward (northward) export of OMHT is notably decreased (increases) in ROM in the AS, BoB, and EIO; however, there is an increase in southward export OMHT in the SIO. MPI-ESM mostly overestimates the southward export of OMHT in the AS, BoB, and EIO, whereas, in SIO, these southward exports of OMHT are reduced. Therefore, the seasonal variation of OMHT can also modify the upper-ocean thermal structure in the basin. The decrease in southward export of OMHT in ROM inhibits the export of the ocean's thermal storage out of the basin in all seasons. For AS, the decrease in southward export of OMHT increases the SST by ~1.2°C with the maximum difference (of about ~ 1.6°C) from January to March and minimum difference (of about ~ 0.5°C) during June (Figure 13e). For BoB, from February to May, the reduction of southward export of OMHT increases SST by ~0.5°C – 1.0°C, respectively. But during June to September, a reversal of the southwest monsoon current significantly reduces the southward advection of cold freshwater flux (Figure not shown), leads to ~1.0°C drop in SST in the basin (Figure 13f). For EIO, the decrease in the magnitude of southward export of OMHT, except June and July, increases the SST by ~ 0.4°C (Figure 13g). However, in the SIO, the increase in southward export of OMHT increases SST by ~0.3°C to ~0.5°C (Figure 13h).

In ROM, the reduction of OMHT restricts the southward export of ocean thermal storage and increases the surface warming by ~4% in the AS basin. Therefore, simulated SST reaches the observed value and reduces the SST error by ~0.2°C to ~0.6°C (Figure 3b). In BoB, the reduction of southward export of OMHT increases the SST error by ~0.1°C – 0.3°C. For EIO, the southward export of OMHT shows an anomalous behaviour from June to July (Figure 12c). In SIO, an increase in the southward export of OMHT increases the surface warming by ~ 1% – 2%, leads to a reduction in SST cold bias (-0.3°C to 0.2°C) and thereby reduces the SST error by ~ 20% – 40% (Figure 3c).

4.7 Annual cycle of meridionally average sea surface height anomaly (SSHA) and ocean surface current (OSC) at a latitudinal belt of 1°S – 1°N

Figure 14 shows the annual cycle of zonally averaged equatorial SSHA from altimeter (ALTI; 1st column of 1st row), MPI-ESM (2nd column of 1st row), and ROM (3rd column of 1st row) while 2nd and 3rd row represents the annual cycle of zonal current and the magnitude of OSC at a latitudinal belt of 1°S – 1°N. In ROM, SSHA has significantly increased by 6m – 8m during April – July and 3m – 4m in August – October compared to ALTI and MPI-ESM run in the EEIO (Figure 14c). This increase in SSHA at the eastern boundary of the equator is due to an increase in the eastward flow of ROM zonal velocity (Figure 14f). As a result, at the eastern boundary of the EIO, the surface remains warm for a longer period and reduces the cold SST bias and thereby reducing the SST error by 5% – 10% (Figure 3c) and ML error by ~20% (Figure 8c) compared to MPI-ESM. Though SSHA of ROM and MPI-ESM are relatively close to the ALTI at the western boundary of the EIO, the strength of the westward flow of zonal velocity (Figure 14f) and the magnitude of OSC (Figure 14i) is much stronger in ROM during June – September. The increase in strength of the westward flow of zonal velocity inhibits the strength of the equatorial counter-current and increases the northward (southward) import (export) of warm surface water at the western boundary of EIO, which increase the warm SST bias by 0.2°C – 0.6°C (Figure 2b) and thereby 20% – 40% increase of SST error off the Somali coast and reduction of SST error in the AS (Figure 3c).

5 Conclusion

The advantages of high-resolution RESM, namely ROM over the low-resolution earth system model (MPI-ESM), were assessed for 1982-2001. The performance of ROM is demonstrated for SST, WT, ML, SWS, OSC, and OMHT for different regions. ROM shows better skill

compared to MPI-ESM in simulating the near-surface and subsurface characteristics of the ocean (e.g. sea surface temperature (SST), subsurface temperature, and mixed layer (ML). However, larger added values are noticed for subsurface (deeper than 350m) thermal structure. It is observed that ROM reduces the SST cold bias from –0.93°C to +0.26°C over AS, –0.4°C to –0.25°C over EIO and –0.32°C to –0.01°C over SIO, however, a strong cold bias of –0.6°C is observed over the BoB. The improvement (added value) is observed over most parts of the TIO with varying degrees of magnitude ~0.2°C – 1.4°C (for SST) and ~5m – 15m (for ML). Seasonal climatology of the ocean's meridional heat transport (OMHT) is also investigated for different regions. OMHT transport in ROM is consistent with the improvement in SST. For example, reduced southward export of OMHT over AS increases the surface warming by ~4%, reducing the RMSE by ~0.2°C to ~0.6°C and becoming closer to observation. This is in good agreement that the reduction of basin-average OMHT increases surface warming and improves the SST simulation in the north TIO (Mallick et al., 2020). The error in EEIO may be due to a strong equatorial mixing and weaker export/import of the heat out of the region. However, in the SIO, the southward export of OMHT value is increased by 1.0 PW, as a result, this reduces average SST error by ~13%. The reduction in the cold SST biases in ROM is also associated with the shoaling of ML due to the weaker Surface wind stress (SWS) which amplifies upper-ocean heat and hence warming.

It can be thus suggested that using high-resolution RESM, one can expect a better simulation near-surface thermal structure with reduction of cold SST bias over TIO. This further suggests that improvement in the upper ocean thermal structure improves the ML dynamics. Therefore, a high-resolution coupled model is ideal for understanding the coupled climate phenomena over TIO.

Acknowledgement

Data Availability Statement

The observational datasets used in this study are derived from the following URL, and model data would be made available upon request to the corresponding author.

References

Abram, N. J., Gagan, M. K., Cole, J. E., Hantoro, W. S., & Mudelsee, M. (2008). Recent intensification of tropical climate variability in the Indian Ocean. *Nat. Geosci.*, **1**, 849–853.

Amaya, D. J., Alexander M. A., Capotondi, A., Deser C., Karnauskas, K. B., Miller, A. J., Mantua. N. J. Are long-term changes in mixed layer depth influencing North Pacific marine heatwaves? In "explaining extremes of 2019 from a climate perspective" Bull. Am. Meteorol. Soc., 102 (1) (2021), pp. S59-S66, 10.1175/BAMS-D-20-0144.1

Annamalai, H., & Murtugudde, R. (2004). Role of the Indian ocean in regional climate variability. *Geophysical Monograph Series*, Vol. 147 of, Blackwell Publishing Ltd, 213–246.

Behera, S. K., Krishnan, R., & Yamagata, T. (1999). Unusual ocean-atmosphere conditions in the tropical Indian Ocean during 1994. *Geophys. Res. Lett.*, **26**, 3001–3004. https://doi.org/10.1029/1999GL010434.

Bellon, G., Sobel, A. H., & Vialard, J. (2008). Ocean-atmosphere coupling in the monsoon intraseasonal oscillation: A simple model study. *J. Clim.*, **21**, 5254–5270. https://doi.org/10.1175/2008JCLI2305.1.

Benshila, R., Durand, F., Masson, S., Bourdallé-Badie, R., de Boyer Montégut, C., Papa, F., & Madec, G. (2014). The upper Bay of Bengal salinity structure in a high-resolution model. *Ocean Model.*, **74**, 36–52. https://doi.org/10.1016/j.ocemod.2013.12.001.

Bonjean, F., & Lagerloef, G. S. E. (2002). Diagnostic model and analysis of the surface currents in the Tropical Pacific Ocean. *J. Phys. Oceanogr.*, **32**, 2938–2954. https://doi.org/10.1175/1520-0485(2002)032<2938:DMAAOT>2.0.CO;2.

Cai, W., Santoso, A., Wang, G., Weller, E., Wu, L., Ashok, K., Masumoto, Y., & Yamagata, T. (2014). Increased frequency of extreme Indian ocean dipole events due to greenhouse warming. *Nature*, **510**, 254–258. https://doi.org/10.1038/nature13327.

Chassignet, E. P., & Coauthors. (2020). Impact of horizontal resolution on global ocean-sea ice model simulations based on the experimental protocols of the Ocean Model Intercomparison Project phase 2 (OMIP-2). *Geosci. Model Dev.*, **13**, 4595–4637. https://doi.org/10.5194/gmd-13-4595-2020.

Delworth, T. L., & Coauthors. (2012). Simulated climate and climate change in the GFDL CM2.5 high-resolution coupled climate model. *J. Clim.*, **25**, 2755–2781. https://doi.org/10.1175/JCLI-D-11-00316.1.

Deppenmeier, A. L., Haarsma, R. J., LeSager, P., & Hazeleger, W. (2020). The effect of vertical ocean mixing on the tropical Atlantic in a coupled global climate model. *Clim. Dyn.*, **54**, 5089–5109. https://doi.org/10.1007/s00382-020-05270-x.

Dong, L., Zhou, T., & Wu, B., (2014). Indian Ocean warming during 1958-2004 simulated by a climate system model and its mechanism. *Clim. Dyn.*, **42**, 203–217. https://doi.org/10.1007/s00382-013-1722-z.

Dubey, A. K., Lal, P., Kumar, P., Kumar, A., & Dvornikov, A. Y. (2021). Present and future projections of heatwave hazard-risk over India: A regional earth system model assessment. *Environmental Research*, *201*, 111573.

Duvel, J. P., Roca, R., & Vialard, J. (2004). Ocean mixed layer temperature variations induced by intraseasonal convective perturbations over the Indian Ocean. *J. Atmos. Sci.*, **61**, 1004–1023. https://doi.org/10.1175/1520-0469(2004)061<1004:OMLTVI>2.0.CO;2.

Dwivedi, S., Srivastava, A., & Mishra, A. K. (2018). Upper Ocean Four-Dimensional Variational Data Assimilation in the Arabian Sea and Bay of Bengal. *Mar. Geod.*, **41**, 230–257. https://doi.org/10.1080/01490419.2017.1405128.

Dwivedi, S., Mishra, A. K., & Srivastava, A. (2019). Upper ocean high resolution regional modeling of the Arabian Sea and Bay of Bengal. *Acta Oceanol. Sin.* 38, 32–50. https://doi.org/10.1007/s13131-019-1439-x

Fischer, A. S., Terray, P., Guilyardi, E., Gualdi, S., & Delecluse, P. (2005). Two independent triggers for the Indian Ocean dipole/zonal mode in a coupled GCM. *J. Clim.*, **18**, 3428–3449. https://doi.org/10.1175/JCLI3478.1.

Gadgil, S., Joseph, P. V., &Joshi, N. V. (1984). Ocean-atmosphere coupling over monsoon regions. *Nature*, **312**, 141–143. https://doi.org/10.1038/312141a0.

Griffies, S. M. (1998). The Gent-McWilliams skew flux. *J. Phys. Oceanogr.*, **28**, 831–841. https://doi.org/10.1175/1520-0485(1998)028<0831:TGMSF>2.0.CO;2.

Hagemann, S., &Dümenil, L. (1997). A parametrization of the lateral waterflow for the global scale. *Clim. Dyn.*, **14**, 17–31. https://doi.org/10.1007/s003820050205.

Hu, S., & Fedorov, A. V. (2019). Indian Ocean warming can strengthen the Atlantic meridional overturning circulation. *Nat. Clim. Chang.*, **9**, 747–751. https://doi.org/10.1038/s41558-019-0566-x.

Huang, G., Qu, X. & Hu, K. (2011). The impact of the tropical Indian Ocean on South Asian High in boreal summer. *Adv. Atmos. Sci.*, **28**, 421–432. https://doi.org/10.1007/s00376-010-9224-y.

Huang, K., Derada, S., Xue, H., Xiu, P., Chai, P., Xie, Q., & Wang, D. (2015). A 1/8° coupled biochemical-physical Indian Ocean Regional Model: Physical results and validation. *Ocean Dyn.*, **65**, 1121–1142. https://doi.org/10.1007/s10236-015-0860-8.

Jacob, D. (2001). A note to the simulation of the annual and inter-annual variability of the water budget over the Baltic Sea drainage basin. *Meteorol. Atmos. Phys.*, **77**, 61–73. https://doi.org/10.1007/s007030170017.

Jungclaus, J. H., & Coauthors. (2006). Ocean circulation and tropical variability in the coupled model ECHAM5/MPIOM. *J. Clim.*, **19**, 3952–3972. https://doi.org/10.1175/JCLI3827.1.

Klingaman, N. P., Woolnough, S. J., Weller, H., & Slingo, J. M. (2011). The impact of finer-resolution air-sea coupling on the intraseasonal oscillation of the Indian monsoon. *J. Clim.*, **24**, 2451–2468. https://doi.org/10.1175/2010JCLI3868.1.

Kumar, P., Mishra, A.K., Dubey, A. K., Javed, A., Saharwardi, M. S., Kumari, A., Sachan, D., Cabos, W., Jacob, & Sein, D. V. (2022). Regional Earth System Modelling Framework for CORDEX-SA: An integrated model assessment for Indian summer monsoon rainfall. C*limate Dynamics***.**10.1007/s00382-022-06217-0.

Lau, W. K. M., & Waliser, D. E. (2011). *Intraseasonal variability in the atmosphere-ocean climate system*. Springer Science & Business Media. https://doi.org/10.1007/b138817

Ma, Y., Zhou, X., Bi, D., Sun, Z., & Hirst, A. C. (2015). Improved air–sea flux algorithms in an ocean–atmosphere coupled model for simulation of global ocean SST and its tropical Pacific variability. *Clim. Dyn.*, **44**, 1473–1485. https://doi.org/10.1007/s00382-014-2281-7.

Mallick, S. K., Agarwal, N., Sharma, R., Prasad, K. V. S. R., & Ramakrishna, S. S. V. S. (2020). Thermodynamic Response of a High-Resolution Tropical Indian Ocean Model to TOGA COARE Bulk Air–Sea Flux Parameterization: Case Study for the Bay of Bengal (BoB). *Pure Appl. Geophys.*, **177**, 4025–4044. https://doi.org/10.1007/s00024-020-02448-6.

Marsland, S. J., Haak, H., Jungclaus, J. H., Latif, M., &Röske, F. (2003). The Max-Planck-Institute global ocean/sea ice model with orthogonal curvilinear coordinates. *Ocean Model.*, **5**, 91–127. https://doi.org/10.1016/S1463-5003(02)00015-X.

Mishra, A. K., Dwivedi, S., &Das, S. (2020). Role of Arabian Sea warming on the Indian summer monsoon rainfall in a regional climate model. *Int. J. Climatol.*, **40**, 2226–2238. *https://doi.org/10.1002/joc.6328.*

Mishra, A. K., Dwivedi, S., & Di Sante, F. (2021a). Performance of the RegCM-MITgcm Coupled regional model in simulating the Indian summer monsoon rainfall. *Pure and Applied Geophysics*. DOI: 0.1007/s00024-020-02648-0.

Mishra, A. K., Kumar, P., Dubey, A. K., Javed, A., Saharwardi, M. S., Sein, D. V., Martyanov, S., & Jacob, D. (2021b). Impact of horizontal resolution on monsoon precipitation for CORDEX-South Asia: A regional earth system model assessment. Atmospheric Research, p.105681.doi.org/10.1016/j.atmosres.2021.105681

Mishra, A.K., Dubey, A. K., & S. Das S. (2022c). Identifying the changes in winter monsoon characteristics over Indian subcontinents due to Arabian Sea warming. Atmospheric Research,. 10.1007/s00382-022-06249-6

Mishra, A. K., Kumar, P., Dubey, A. K., Jha, S. K., Sein, D. V., & Cabos W. (2022b) Demonstrating the asymmetry of the Indian Ocean Dipole response in the Regional Earth System model of CORDEX-SA. Atmospheric Research, 273:106182. https://doi.org/10.1016/j.atmosres.2022.106182.

Mishra, A. K., Kumar, P., Dubey, A. K., Tiwari, G., & Sein, D. V., (2022c). Impact of air-sea coupling on the simulation of Indian summer monsoon using a high-resolution Regional Earth System Model over CORDEX-SA. Climate Dynamics. http://dx.doi.org/10.1007/s00382-022-06249-6

Pandey, L. K., & Dwivedi, S. (2021). Comparing the Performance of Turbulent Kinetic Energy and K-Profile Parameterization Vertical Parameterization Schemes over the Tropical Indian Ocean. Mar. Geod., 44, 42–69. https://doi.org/10.1080/01490419.2020.1835758.

Prasad, T. G. (2004). A comparison of mixed-layer dynamics between the Arabian Sea and Bay of Bengal: One-dimensional model results. *J. Geophys. Res. Ocean.*, **109.** https://doi.org/10.1029/2003jc002000.

Praveen K. B., Vialard, J., Lengaigne, M., Murty, V. S. N., McPhaden, M. J., Cronin, M. F., Pinsard, F., & Reddy, K. G. (2013). TropFlux wind stresses over the tropical oceans: Evaluation and comparison with other products. *Clim. Dyn.*, **40**, 2049–2071. https://doi.org/10.1007/s00382-012-1455-4.

Reynolds, R. W., Smith, T. M., Liu, C., Chelton, D. B., Casey, K. S., & Schlax, M. G. (2007). Daily high-resolution-blended analyses for sea surface temperature. *J. Clim.*, **20.** 5473–5496, https://doi.org/10.1175/2007JCLI1824.1.

Roxy, M. K., Ritika, K., Terray, P., &Masson, S. (2014). The curious case of Indian Ocean warming. *J. Clim.*, **27**, 8501–8509. https://doi.org/10.1175/JCLI-D-14-00471.1.

Saharwardi, M. S., Kumar, P., & Sachan, D. (2021). Evaluation and projection of drought over India using high-resolution regional coupled model ROM, Climate dynamics, **58**, 503-521. https://doi.org/10.1007/s00382-021-05919-1

Saji, N. H., Goswami, B. N., Vinayachandran, P. N., &Yamagata, T. (1999). A dipole mode in the tropical Indian ocean. *Nature*, **401**, 360–363. https://doi.org/10.1038/43854.

Samson, G., & Coauthors. (2015). The NOW regional coupled model: Application to the tropical Indian Ocean climate and tropical cyclone activity. *J. Adv. Model. Earth Syst.*, **6**, 700–722. https://doi.org/10.1002/2014MS000324.

Schott, F. A., & McCreary, J. P. (2001). The monsoon circulation of the Indian Ocean. *Prog. Oceanogr.*, **51**, 1–123. https://doi.org/10.1016/S0079-6611(01)00083-0.

Schott, F. A., Xie, S. P., & McCreary, J. P. (2009). Indian ocean circulation and climate variability. *Rev. Geophys.*, **47.** https://doi.org/10.1029/2007RG000245.

Sein, D. V., & Coauthors. (2015). Regionally coupled atmosphere-ocean-sea ice-marine biogeochemistry model ROM: 1. Description and validation. *J. Adv. Model. Earth Syst.*, **7**, 268–304. https://doi.org/10.1002/2014MS000357.

Sein, D. V., & Coauthors. (2020). Regionally Coupled Atmosphere-Ocean- Marine Biogeochemistry Model ROM: 2. Studying the Climate Change Signal in the North Atlantic and Europe. *J. Adv. Model. Earth Syst.*, **12.** https://doi.org/10.1029/2019MS001646.

Sein, D. V., Dvornikov, A. Y., Martyanov, S. D., et al (2022). Indian ocean marine biogeochemical variability and its feedback on simulated South Asia climate. Earth System Dynamics 13(2): 809–831. DOI: 10.5194/esd-13-809-2022

Sharma, R., Agarwal, N., Chakraborty, A., Mallick, S., Buckley, J., Shesu, V., & Tandon, A. (2016). Large-Scale Air-Sea Coupling Processes in the Bay of Bengal Using Space-Borne Observations. *Oceanography*, **29**, 192–201. https://doi.org/10.5670/oceanog.2016.51.

Shroyer, E., D. Rudnick, J. T. Farrar, B. Lim, S. K. Venayagamoorthy, L. St. Laurent, A. Garanaik, and J. Moum, (2016): Modification of Upper-Ocean Temperature Structure by Subsurface Mixing in the Presence of Strong Salinity Stratification. *Oceanography*, **29**, 62–71. https://doi.org/10.5670/oceanog.2016.39.

Srivastava, A., Dwivedi, S., & Mishra, A. K. (2016). Intercomparison of High-Resolution Bay of Bengal Circulation Models Forced with Different Winds. *Mar. Geod.*, **39**, 271–289. https://doi.org/10.1080/01490419.2016.1173606.

Srivastava, A., Dwivedi, S., & Mishra, A. K. (2018). Investigating the role of air-sea forcing on the variability of hydrography, circulation, and mixed layer depth in the Arabian Sea

and Bay of Bengal. *Oceanologia*, **60**, 169–186. https://doi.org/10.1016/j.oceano.2017.10.001.

Stathopoulos, C., Galanis, G., & Kallos, G. (2020). A coupled modeling study of mechanical and thermodynamical air-ocean interface processes under sea storm conditions. *Dyn. Atmos. Ocean.*, **91.** https://doi.org/10.1016/j.dynatmoce.2020.101140.

Stevens, B., & Coauthors. (2013). Atmospheric component of the MPI-M Earth System Model: ECHAM6. *J. Adv. Model. Earth Syst.*, **5**, 146–172. https://doi.org/10.1002/JAME.20015@10.1002/(ISSN)1942-2466.MPIESM1.

Storto, A., & Masina, S. (2016). C-GLORSv5: an improved multipurpose global ocean eddy-permitting physical reanalysis. *Earth Syst. Sci. Data*, **8**, 679–696. https://doi.org/10.5194/essd-8-679-2016.

Sun, C., & Coauthors. (2010). The Data Management System for the Global Temperature and Salinity Profile Programme. European Space Agency, 931–938.

Thomas, M., Sündermann, J., & Maier-Reimer, E. (2001). Consideration of ocean tides in an OGCM and impacts on subseasonal to decadal polar motion excitation. *Geophys. Res. Lett.*, **28**, 2457–2460. https://doi.org/10.1029/2000GL012234.

Trenberth, K. E., & Solomon, A. (1994). The global heat balance: heat transports in the atmosphere and ocean. *Clim. Dyn.*, **10**, 107–134. https://doi.org/10.1007/BF00210625.

Valcke, S. (2013) The OASIS3 coupler: a European climate modelling community software. Geosci Model Dev 6:373–388. https://doi.org/10.5194/gmd-6-373-2013

Vinayachandran, P. N., Jahfer, S., & Nanjundiah, R. S. (2015). Impact of river runoff into the ocean on Indian summer monsoon. *Environ. Res. Lett.*, **10**, 54008. https://doi.org/10.1088/1748-9326/10/5/054008.

Wang, S., Dieterich, C., Döscher, R., Höglund, A., Hordoir, R., Meier, H. E. M., Samuelsson, P., & Schimanke, S. (2015). Development and evaluation of a new regional coupled

atmosphere–ocean model in the North Sea and Baltic Sea. *Tellus A Dyn. Meteorol. Oceanogr.*, **67**, 24284. https://doi.org/10.3402/tellusa.v67.24284.

Yamagata, T., Behera, S. K., Luo, J. J., Masson, S., Jury, M. R., &Rao, S. A. (2004). Coupled ocean-atmosphere variability in the tropical Indian ocean. *Geophysical Monograph Series*, Vol. 147 of, Blackwell Publishing Ltd, 189–211.

Yeh, SW., Yim, B.Y., Noh, Y. *et al.* Changes in mixed layer depth under climate change projections in two CGCMs. *Clim Dyn* **33,** 199–213 (2009). https://doi.org/10.1007/s00382-009-0530-y

Zheng, Y., & Giese, B. S. (2009). Ocean heat transport in simple ocean data assimilation: Structure and mechanisms. *J. Geophys. Res. Ocean.*, **114.** https://doi.org/10.1029/2008JC005190.

Table 1: Evaluation model is simulating the sea surface temperature over subregions of India Ocean by performance matrices (ie: RMSE and standard deviation

Region	Root Mean Square Error (RMSE)		Standard Deviation		
	ROM	MPI-ESM-LR	Observation	ROM	MPI-ESM-LR
BoB	0.575	0.691	0.973	0.973	0.974
AS	0.565	1.158	1.163	0.945	1.254
EIO	0.379	0.641	0.60	0.591	0.652
SIO	0.308	0.501	1.07	1.02	1.03

Figures
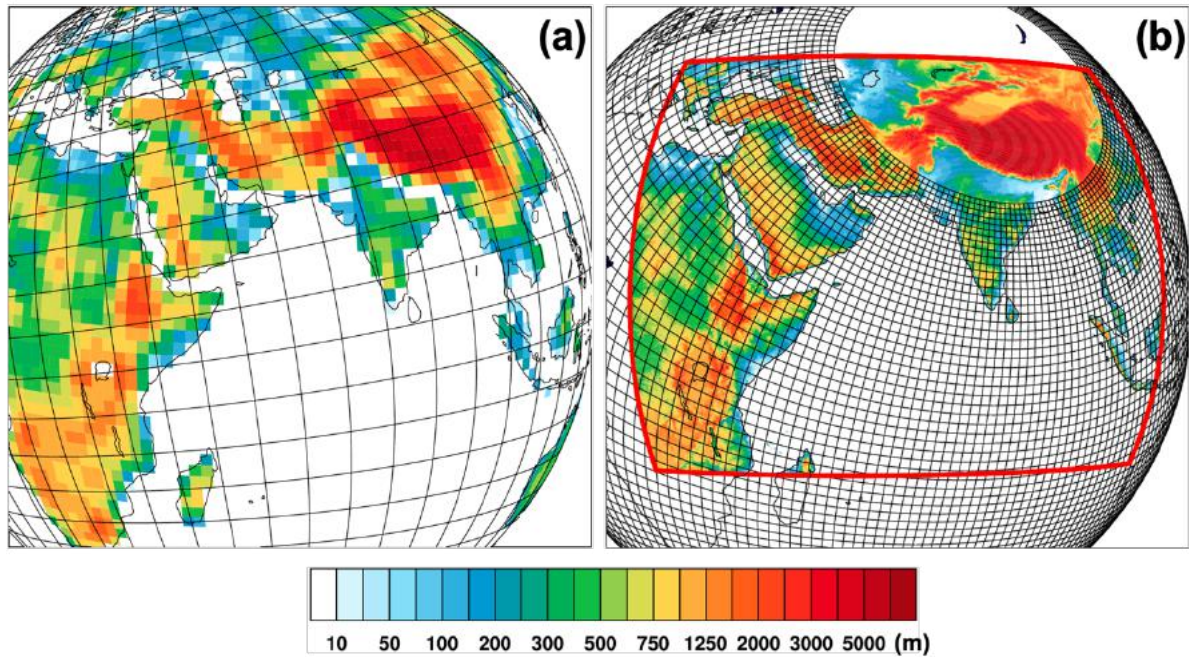
Figure 1. Representation of model grid and orography (shaded color scale) for (a) MPI-ESM and (b) ROM. Solid black lines – MPIOM grid (every 5th grid line is shown). The red rectangle on (b) represents the coupled atmosphere-ocean area in ROM.
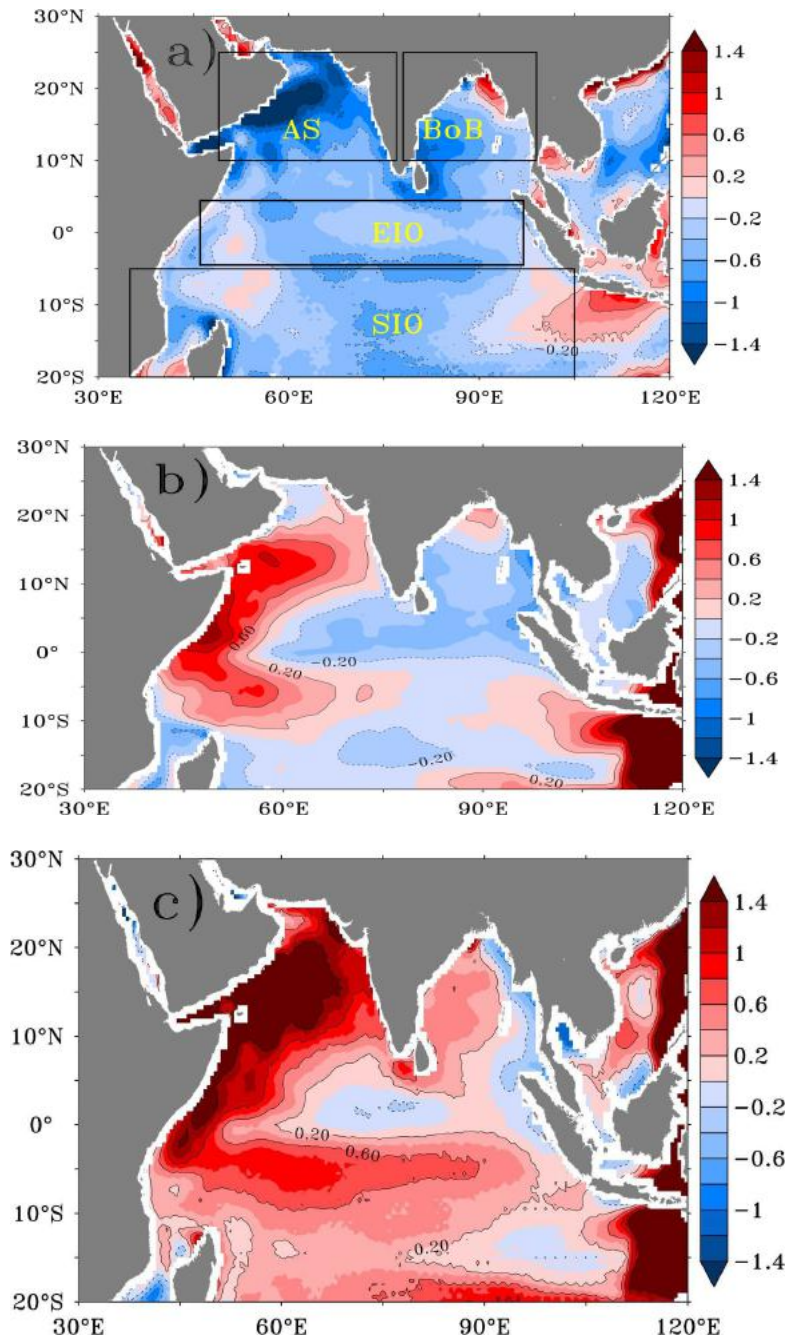
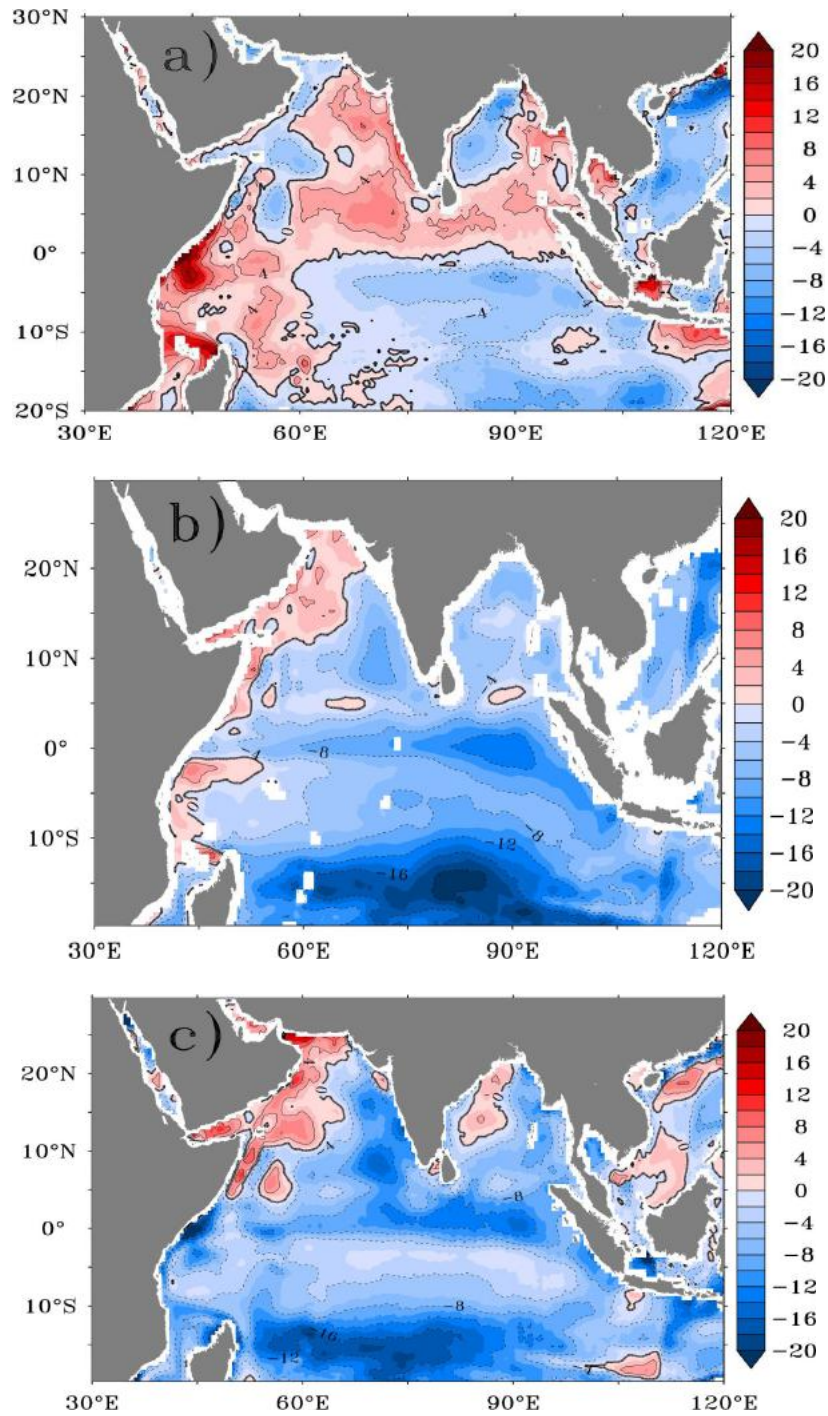**Figure 2:** Spatial distribution of the annual mean SST bias (°C) of (a) MPI-ESM and (b) ROM. (c) Spatial distribution of the time-averaged difference between simulated SSTs (ROM-MPI-ESM) over the period of 1982-2001. SST biases are the time-averaged difference between the simulated SSTs and the Reynolds OI SST.
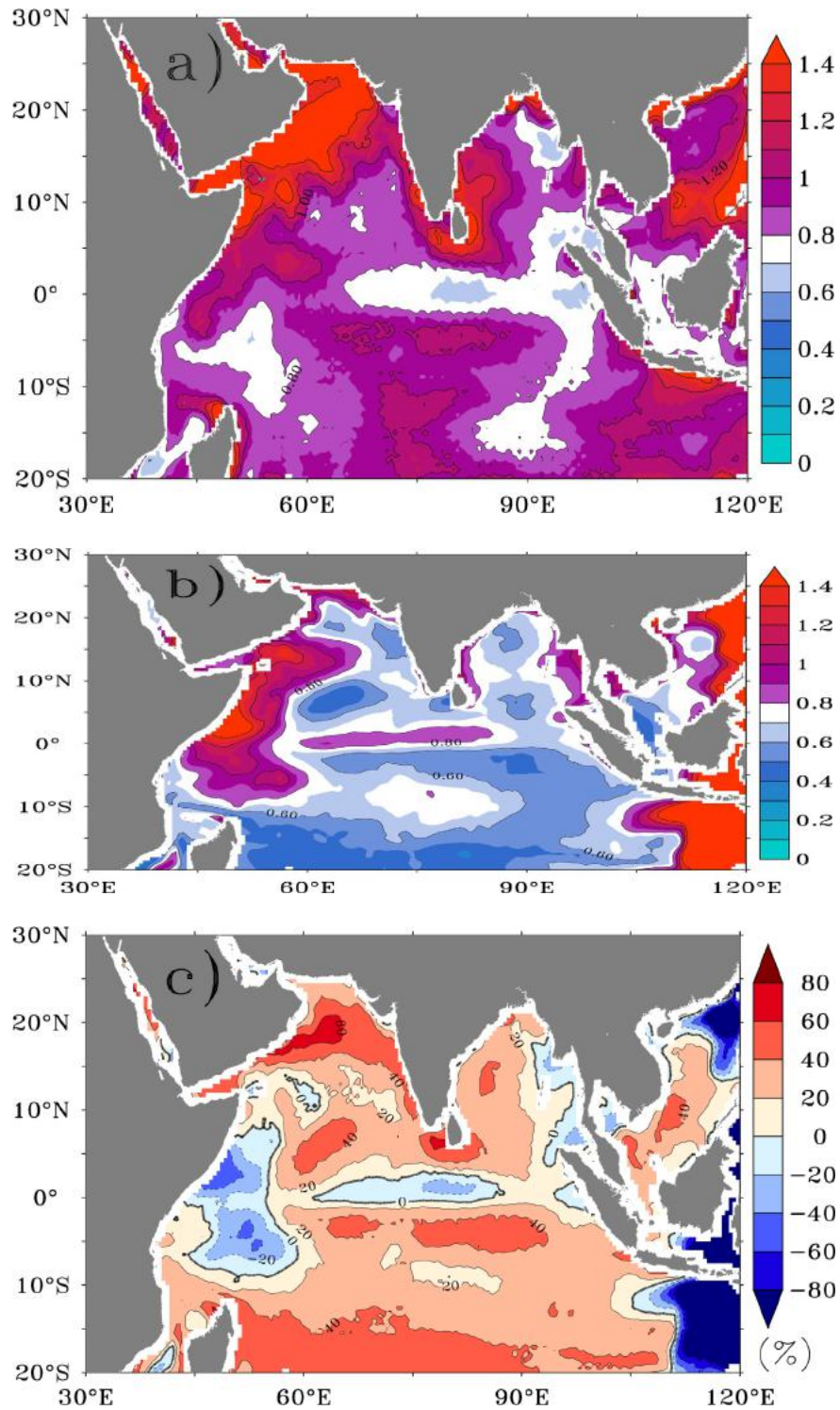
Figure 3: Annual mean simulated sea surface temperature (SST) error (RMSE, °C) from (a) MPI-ESM, (b) ROM with respect to the OISST for the period of 1982-2001. (c) Annual mean SST improvement (positive value) of ROM over MPI-ESM.
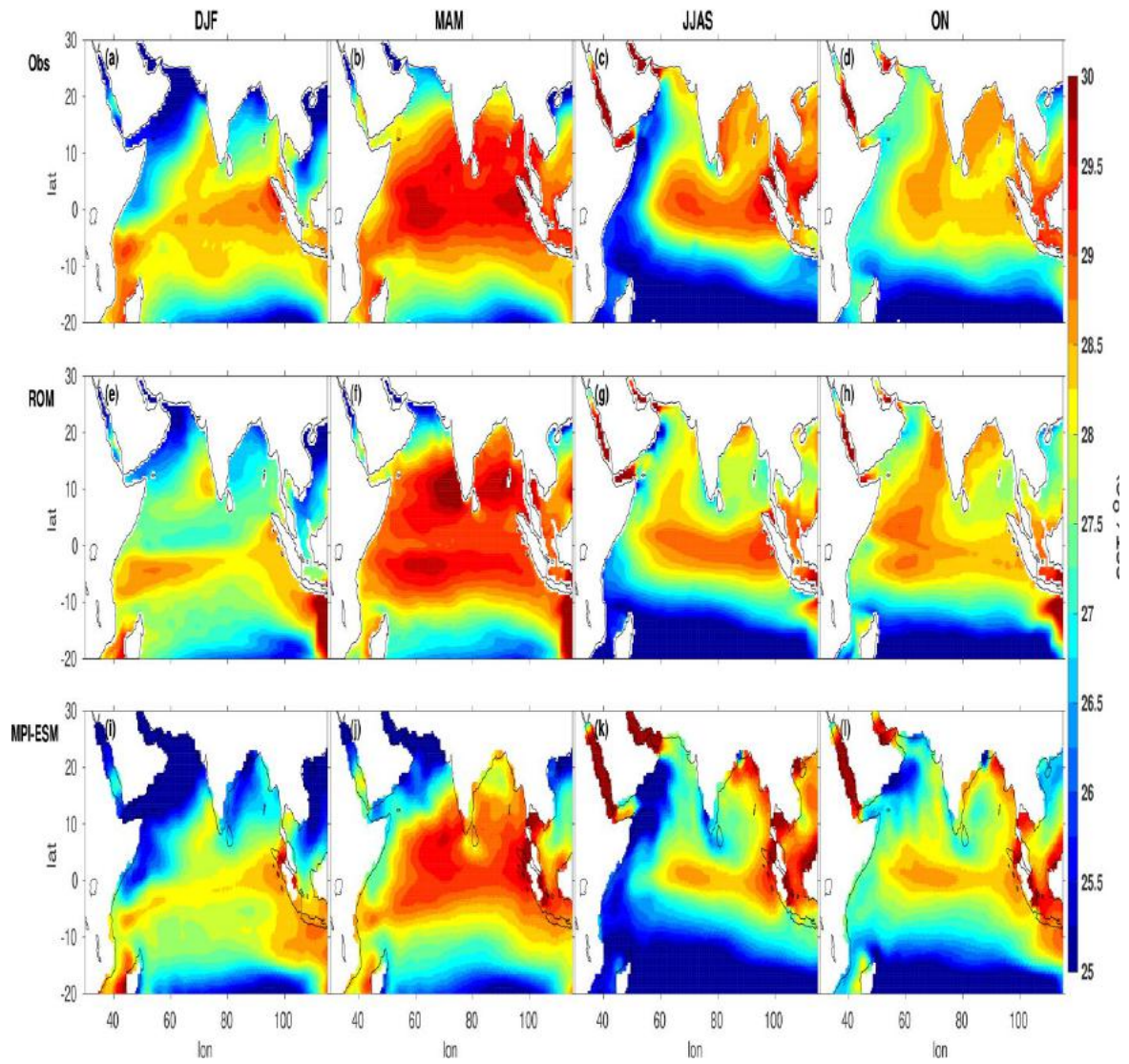
Figure 4: Seasonal mean sea surface temperature (SST in ºC) for observation (Obs), ROM, and MPI-ESM.
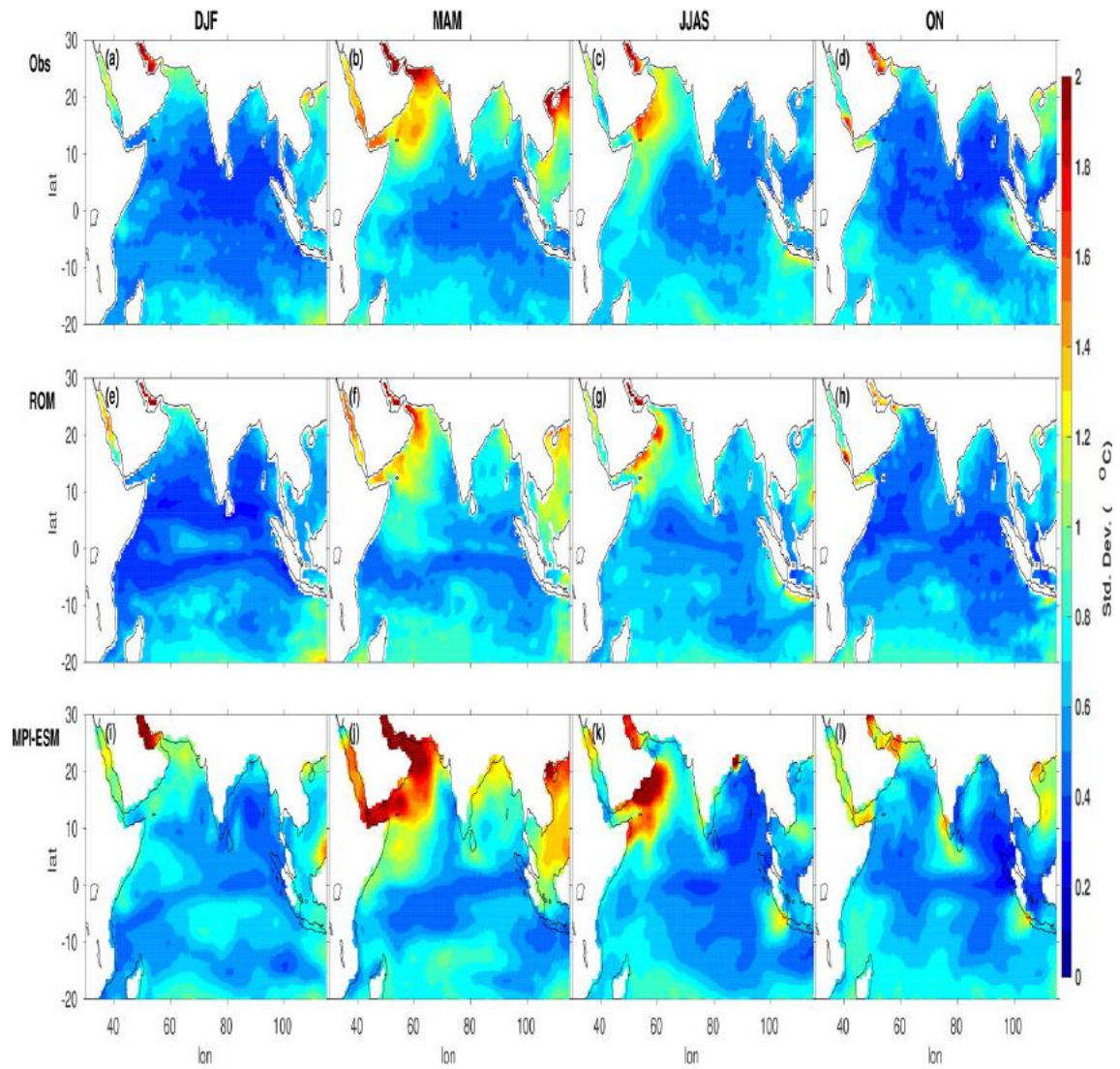
Figure 5: Variability (standard deviation) of sea surface temperature (SST in °C) during each season for observation (Obs), ROM, and MPI-ESM.
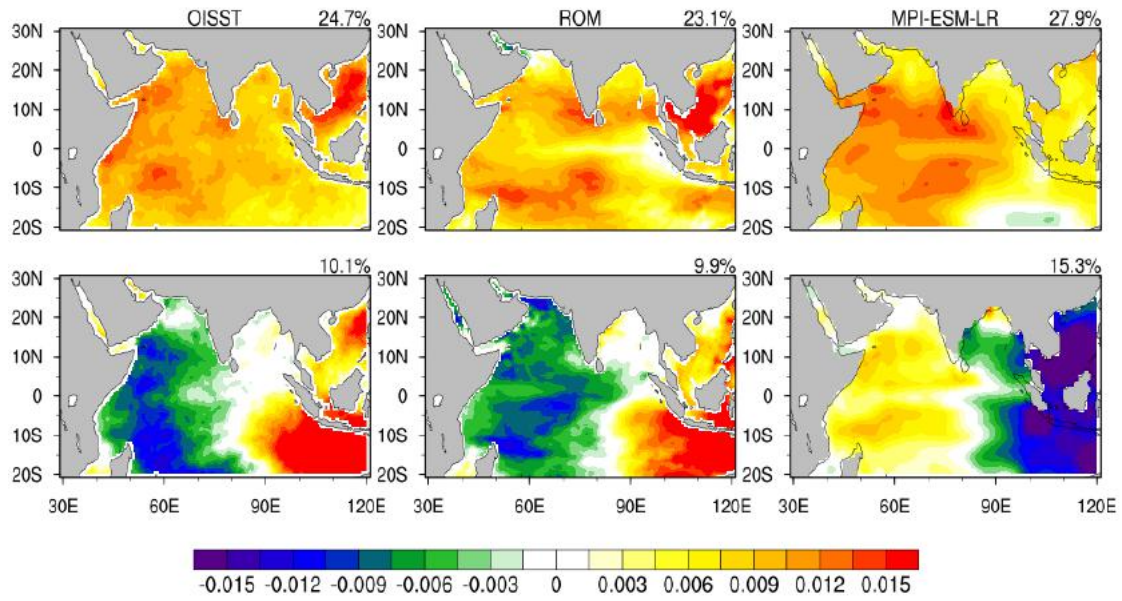
Figure 6: Spatial structure of two leading mode of emperical orthogonal funtion for TIO SST for obsrvation (OISST), ROM and MPI-ESM during 1982-2002: First mode (upper panel) and second mode; lower panel.

Figure 7: Spatial distribution of the annual mean mixed layer (ML in meter) bias (a) MPI-ESM and (b) ROM. and (c) spatial distribution of the time-averaged differences between model ML (ROM -MPI-ESM). ML biases are the time-averaged of the difference between model and computed ML and the C-GLORS ML for 1982-2001.
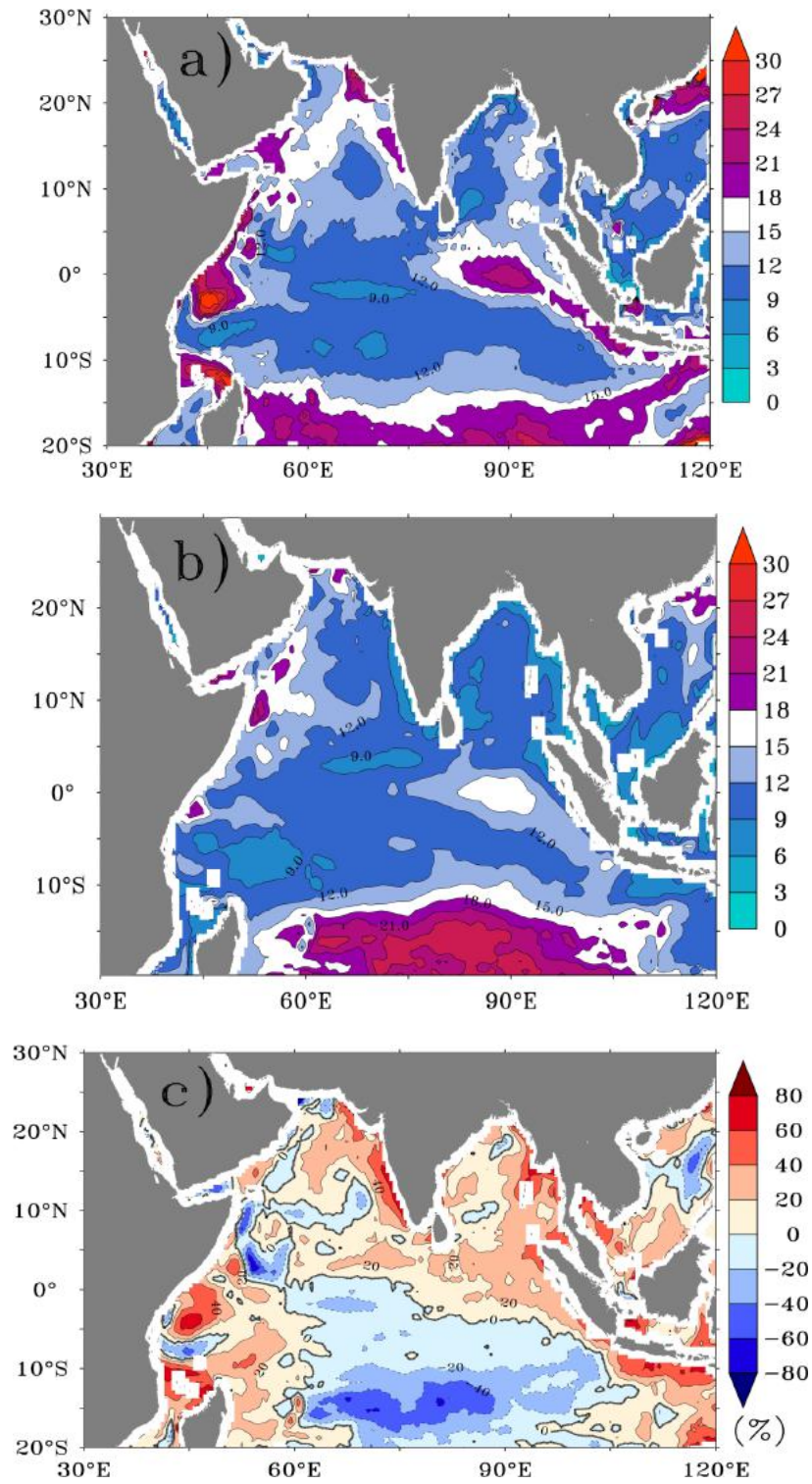
Figure 8: Same as Figure 3 but for mixed layer (ML in meter) error (RMSE, m) of (a) MPI-ESM, and (b) ROM. (c) Annual mean ML improvement (positive value) of ROM over MPI-ESM.
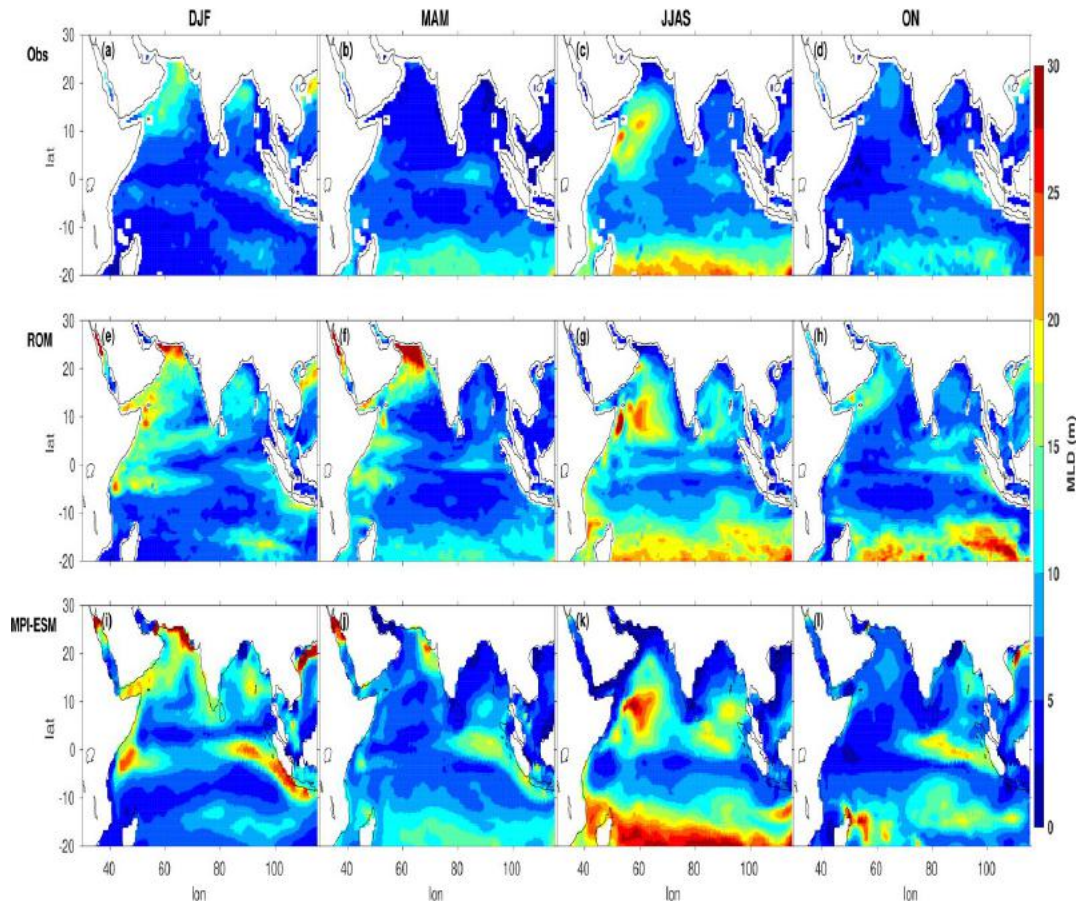
Figure 9: Variability (standard deviation) of mixed layer (in meter) during each season for observation (Obs), ROM, and MPI-ESM.
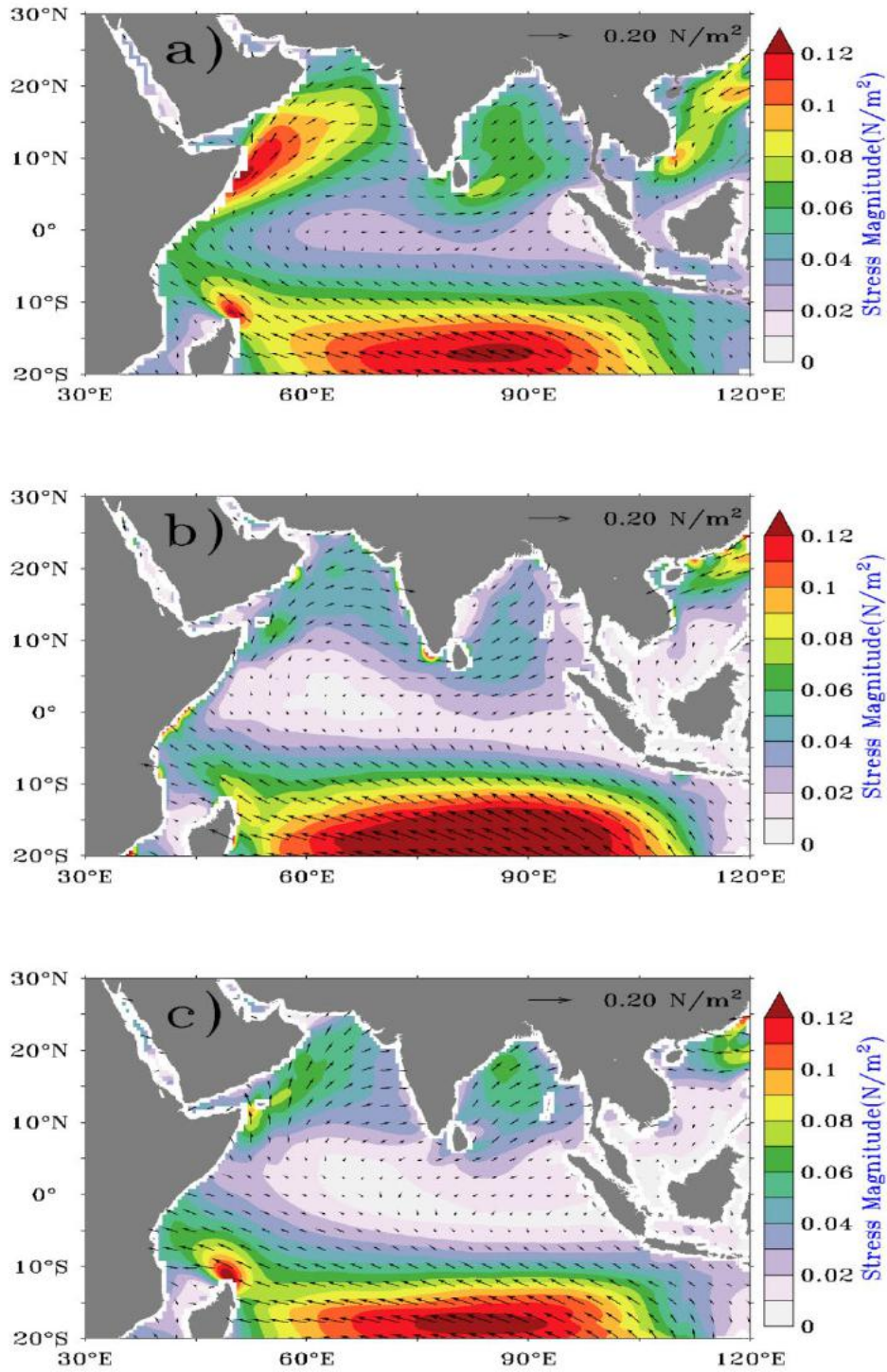
Figure 10: Mean surface momentum flux (N/m 2) with stress vector for the study period from (a) observation (TROPFLUX), (b) MPI-ESM, and (c) ROM run.
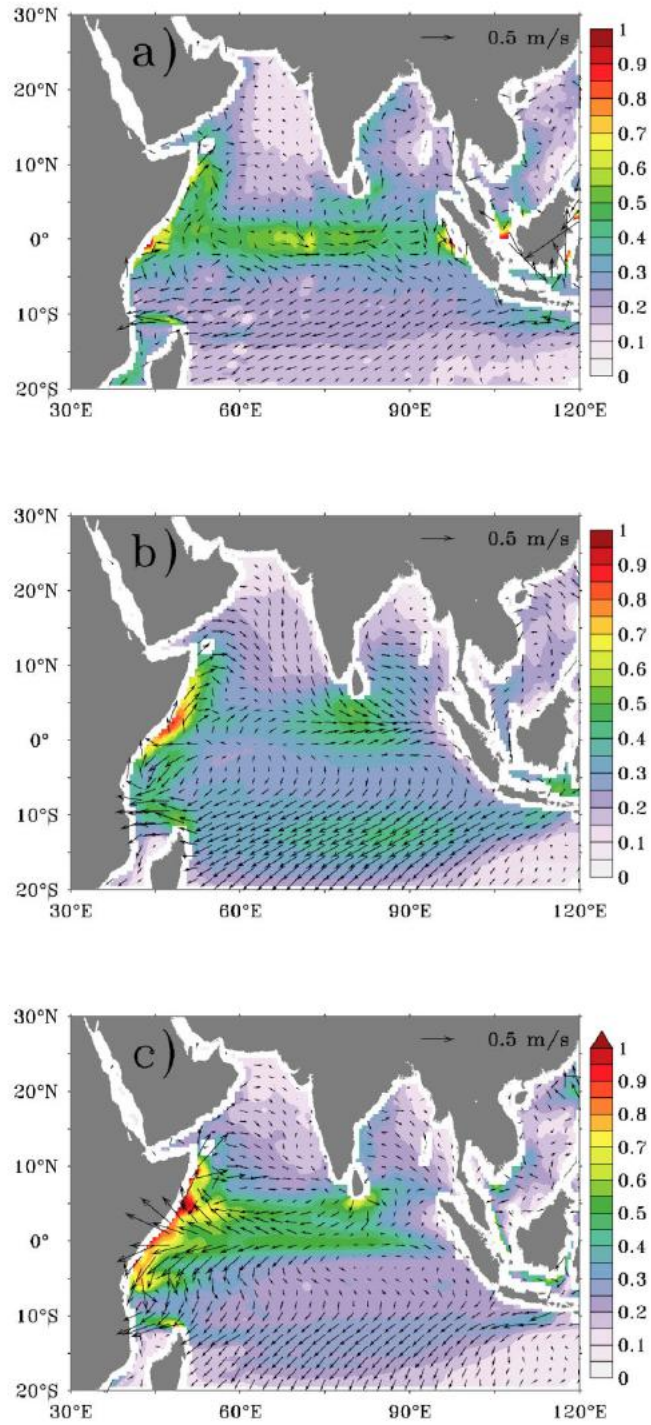
Figure 11: Annual mean current (m/s) with the current vector of (a) ocean surface current

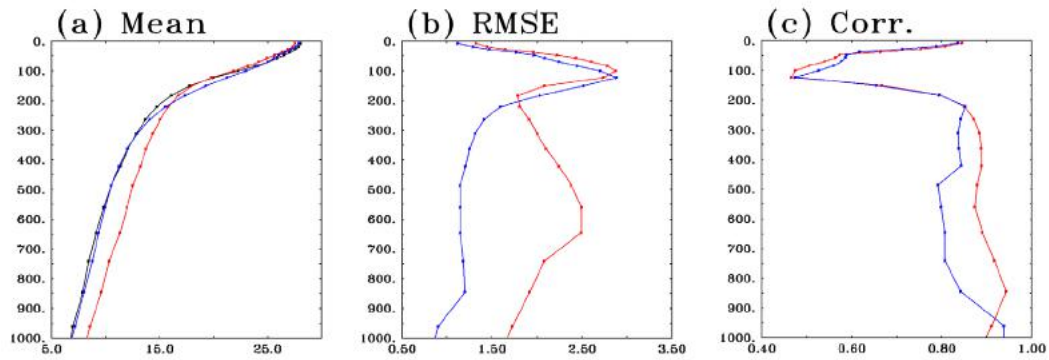analysis real-time (OSCAR), (b) MPI-ESM, and (c) ROM run for the period 1982 – 2001.

Figure 12: Domain averaged statistics of profile (a) mean (°C), (b) root mean square error (RMSE; °C), and (c) correlation for simulated water temperature from MPI-ESM (solid red line with marked squares) and ROM (solid blue line) at 31,159 number of ARGO profiles for the period 1985-2001. Observation (ARGO) is represented as a solid black line with marked squares.
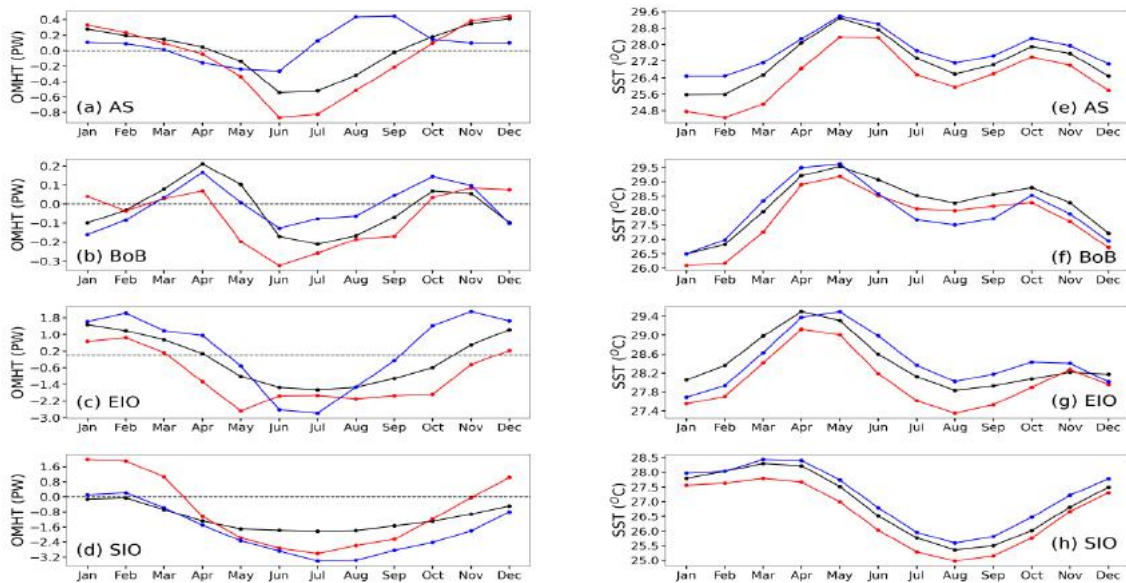

Figure 13: Seasonal cycle of simulated oceans' meridional heat transport (OMHT; Petawatt (PW, $1\,PW = 10^{15}\,W$), left panel; a–d) and the corresponding simulated sea surface temperature (SST in °C, right panel; e–h) from MPI-ESM, ROM and observation over the different regions of TIO. The red line for MPI-ESM, blue line for ROM, and black line for observation.
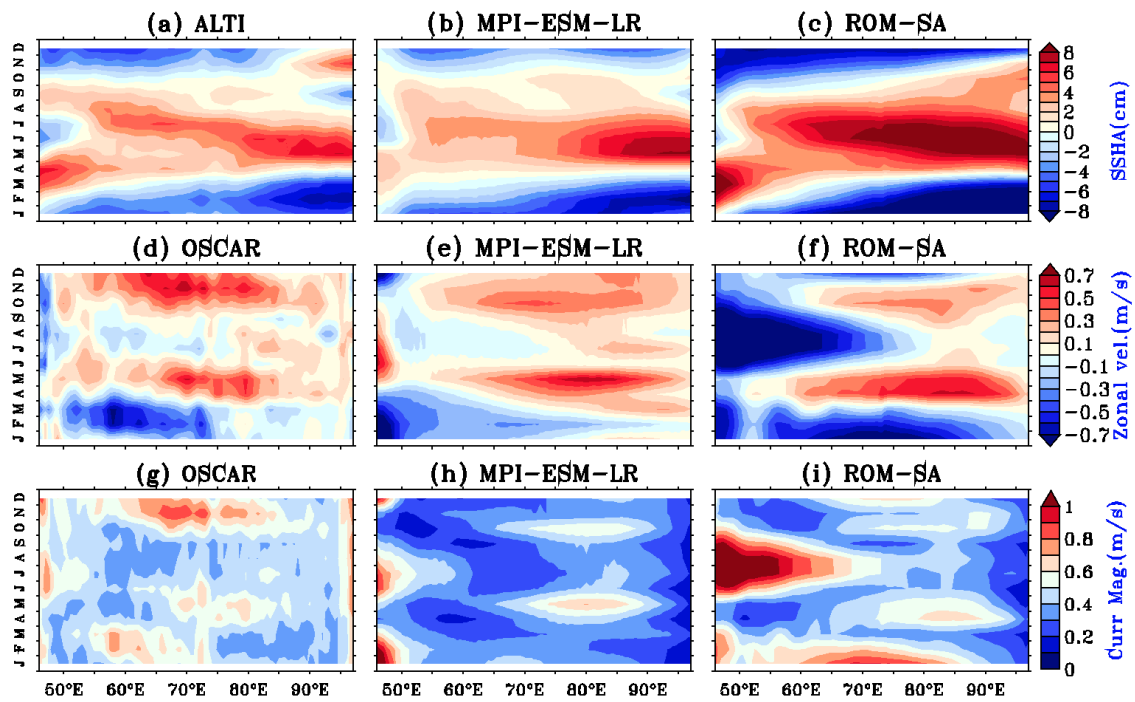
Figure 14: Hovmoller diagram of SSHA (1st row; (a) ALTI, (b) MPI-ESM and (c) ROM; color; cm)), Zonal velocity (2nd row; (d) OSCAR, (e) MPI-ESM and (f) ROM; color; m/s)) and Current magnitude (3rd row; (g) OSCAR, (h) MPI-ESM and (i) ROM; color; m/s)) along an equatorial latitudinal belt (1°S – 1°N).